Evidence for complex iron oxides in the deep mantle from FeNi(Cu) inclusions in super-deep diamond

Chiara Anzolini[a,b], Katharina Marquardt[c,d], Vincenzo Stagno[e,f], Luca Bindi[g], Daniel J. Frost[c], D. Graham Pearson[b], Jeffrey W. Harris[h], Russell J. Hemley[i,j], Fabrizio Nestola[a]

[a]Department of Geosciences, University of Padova, I-35131 Padova, Italy; [b]Department of Earth and Atmospheric Sciences, University of Alberta, T6G 2E3 Edmonton, Canada; [c]Bayerisches Geoinstitut, University of Bayreuth, D-95440 Bayreuth, Germany; [d]now at the Department of Materials, Imperial College London, SW7 2AZ London, United Kingdom; [e]Department of Earth Sciences, Sapienza University of Rome, I-00185 Roma; [f]National Institute of Geophysics and Volcanology, Rome Headquarter, 00143 Roma, Italy; [g]Department of Earth Sciences, University of Firenze, I-50121 Firenze, Italy; [h]School of Geographical and Earth Sciences, University of Glasgow, G12 8QQ Glasgow, United Kingdom; [i]Department of Physics, University of Illinois at Chicago, Chicago, IL 60607, USA; [j]Department of Chemistry, University of Illinois at Chicago, Chicago, IL 60607, USA.

Keywords

Fe_4O_5, ferropericlase, diamond, epigenetic mineral, Earth's mantle.

Author Contributions

The study was conceived by F.N., who also led the research team. C.A. performed the FEG-SEM and EMPA experiments. C.A. and F.N. performed the SCXRD measurements. K.M. performed the TEM analyses. K.M. and F.N. processed the analytical data. F.N., L.B., V.S., C.A., D.J.F., K.M., D.G.P. and R.J.H. wrote the paper. J.W.H. provided the sample. All the authors discussed the results and implications and commented on the manuscript at all stages.

This PDF file includes:

Main Text
Figures 1 to 4

Abstract

The recent discovery in high-pressure experiments of compounds stable to 24-26 GPa with Fe_4O_5, Fe_5O_6, Fe_7O_9, and Fe_9O_{11} stoichiometry has raised new questions about their existence within the Earth's mantle. Incorporating both ferric and ferrous iron in their structures, these oxides if present within the Earth could also provide insight into diamond-forming processes at depth in the planet. Here we report the discovery of metallic particles, dominantly of FeNi ($Fe_{0.71}Ni_{0.24}Cu_{0.05}$), in close spatial relation with nearly pure magnetite grains from a so-called super-deep diamond from the Earth's mantle. The microstructural relation of magnetite within a ferropericlase $(Mg_{0.60}Fe_{0.40})O$ matrix suggests exsolution of the former. Taking into account the bulk chemistry reconstructed from the FeNi(Cu) alloy, we propose that it formed by decomposition of a complex metal *M* oxide (M_4O_5) with a stoichiometry of $(Fe^{3+}_{2.15}Fe^{2+}_{1.59}Ni^{2+}_{0.17}Cu^{+}_{0.04})_{\Sigma=3.95}O_5$. We further suggest a possible link between this phase and variably oxidized ferropericlase that is commonly trapped in super-deep diamond. The observation of FeNi(Cu) metal in relation to magnetite exsolved from ferropericlase is interpreted as arising from a multistage process that

starts from diamond encapsulation of ferropericlase followed by decompression and cooling under oxidized conditions, leading to the formation of complex oxides such as Fe_4O_5 that subsequently decompose at shallower *P-T* conditions.

Significance Statement

Diamonds are among the most important samples of the solid Earth owing to the unique information they provide about the Earth's interior. New analytical techniques have enabled the discovery of distinct inclusions in diamond hosts having mineral associations that constrain the mineralogy of the deep unexplorable Earth. Currently, experimental studies are revealing the stability of novel iron oxides not found at Earth's surface but that would be present in the mantle. We combine textural and chemical analyses on ferropericlase inclusions contained in a diamond sample and demonstrate that the observed association of magnetite + FeNi metal exsolved from the matrix results from post-entrapment decomposition at the expense of a natural Fe_4O_5 phase recently discovered and characterized in high-pressure experiments.

Main Text

Introduction

Sub-lithospheric diamond is an exceptionally rare category of diamond, representing ~1% of the total abundance (1), that crystallized at depths between ~300 km and perhaps greater than ~1000 km (2–5). Also called super-deep diamond (SDD), these are distinguished from more common lithospheric diamond that forms in shallower regions between ~120 km and ~250 km depth (1). In the last decade, these extraordinary diamond samples and their mineral and fluid inclusions have yielded new insights into the interior of our planet (2–5, 6–8). Although this diamond can trap fragments of deep Earth materials, it remains uncertain whether trapped minerals represent surrounding rocks and reflect the local mantle pressure-temperature-oxygen fugacity (*P-T-f*O_2) conditions. Slivers of metallic iron-nickel and iron carbides surrounded by reducing gases (CH_4 and H_2) in unusually large SDD crystals have been recently reported (4). This finding was interpreted as evidence for their growth from liquid metal within highly reducing deep mantle regions between ~300 km and ~1000 km depth. Further, the observation represents the first natural evidence of a process that was previously only observed in high-pressure experiments on the relevant minerals at conditions of deep mantle saturation by a Fe(Ni) metal phase (9). A similar conclusion has been reached for boron-bearing super-deep diamond crystals from several localities around the world (7). In contrast, experimental studies as well as geophysical and geochemical evidence confirm that inclusions of CO_2-bearing minerals and melts provide strong support of the passage of oxidized fluids (6, 10–12). Such observations suggest a mantle redox state varying between reduced conditions, where metallic Fe and diamond can occur together (*f*O_2 ~ iron-wüstite (IW) buffer (9)), and more oxidized conditions that allow the coexistence of diamond and carbonates (either solid or liquid; *f*O_2 ~ IW > + 2 log units (11, 13, 14)).

Investigations of Mg-Fe oxides trapped in SDDs to date have revealed a diverse suite of minerals that can be summarized by the MgO-FeO-Fe_2O_3 ternary diagram, with ferropericlase being the most abundant phase:

ferropericlase inclusions are the most abundant inclusions in SDDs and account for 50-56% of all identified lower-mantle inclusions (12), despite the fact that constraints obtained from computational studies to date indicate that ferropericlase should only comprise ~17% of the lower mantle (15). Ferropericlase inclusions have been linked to the presence of Fe metal in the deep mantle. However, their wide range in Fe# suggests either local chemical heterogeneities (16, 17) or kinetically controlled chemical (redox) reactions that promote the encapsulation of ferropericlase during diamond formation (6, 18–20). Ref. (16) first identified magnesioferrite exsolved from ferropericlase, then confirmed in a number of studies (19, 21–24), and estimated it to be 6-7 vol.% of the original mineral. A similar estimate has been made on the same sample examined in the present study (25). Nanometer-scale investigations using transmission electron microscopy (TEM) revealed the presence of magnesioferrite within a $(Fe_{0.65}Mg_{0.35})O$ magnesiowüstite included in a SDD (21). These authors stated that magnesioferrite comprised ~5-7% of a wüstite component and precipitated either on dislocations or at the interface with diamond. In the same work, blebs of FeNi and rare 20-50 nm sized magnetite exsolutions were also reported. The presence of small amount of Cu was also detected in Fe-Ni, although it was attributed to secondary X-rays from the copper TEM grid (21).

Magnesioferrite has also been observed along with carbonated mineral assemblages, indicating the important role of high fo_2 conditions on the initial bulk Fe^{3+} content (26). Spinel exsolutions in $(Mg_{0.83}Fe_{0.17})O$ ferropericlase such as magnesioferrite that are relatively enriched in Cr and Al have been reported (23). The observed epitaxial growth relationships with ferropericlase suggested these spinel inclusions had exsolved from the matrix where nucleation was facilitated at dislocations (23), in agreement with Refs. (16, 21). Consistent with the observations for SDD ferropericlase inclusions, experiments showing the formation of magnesioferrite on decomposition of Fe^{3+}-rich bridgmanite at 24 GPa have been explained as a consequence of saturation in ferric iron due to decompression (27). The formation of magnesioferrite thus appears to be related to the abundance of Fe^{3+} in the matrix. Finally, experimental studies of the synthesis of ferropericlase focused on the formation of magnesioferrite as an exsolution product due to either an increase in the fo_2 of annealing or the effect of cooling have been reported (28 and references therein).

Recent experiments performed at temperatures between ~1500 and ~2000 K and pressures from 8 to 22 GPa have succeeded in synthesizing several new mixed-valence Fe-oxides with various stoichiometries along the FeO-Fe_3O_4 join (29, 30), such as the orthorhombic-structured phases Fe_4O_5 (29) and Fe_5O_6 (31), and the monoclinic-structured phases Fe_7O_9 (32) and Fe_9O_{11} (33). The finding of these new compounds raised the possibility that several iron oxides with different stoichiometries may be stable at conditions corresponding to the deep Earth's mantle. Interestingly, Fe_4O_5 and Fe_5O_6 have been both shown to form solid solutions with Mg and Cr counterparts and to coexist with silicate phases at the high *P-T* conditions expected in the transition zone of the mantle, including wadsleyite and ringwoodite (34). In addition, these phases can incorporate Fe^{3+} in their structure implying, therefore, a role in redox-driven processes such as diamond formation. The oxygen fugacity (fo_2) is a key variable affecting the stability of carbon, for instance, either as diamond or carbonate (solid or melt). Whether these oxide phases can locally buffer the fo_2 in the deep mantle will depend on the effect that Fe^{3+} has on their stability. Experimental studies supported by thermodynamic calculations have shown that Fe_4O_5 and Fe_5O_6 can be stable at redox conditions where carbonate and diamond, respectively, are stable along with the more abundant silicate minerals (35, 36).

However, to date, no diamond samples have shown evidence of the presence of Fe_xO_y minerals trapped as inclusions.

Here we report the direct observation of FeNi(Cu) metallic particles in close spatial relation with nearly pure magnetite grains trapped in two $(Mg_{0.60}Fe_{0.40})O$ ferropericlase inclusions within a super-deep diamond. Textural and chemical analyses combined with the reconstructed bulk chemistry provide a clear evidence of decomposition of complex metal Fe-O oxides.

Results

The $(Mg_{0.60}Fe_{0.40})O$ ferropericlase inclusions from a super-deep diamond from Juina, Mato Grosso State, Brazil (Fig. 1a) were examined. The diamond crystallized at a minimum calculated pressure of 15.7 (±2.5) GPa at 1830 (±45) K (25), and contains exsolutions of magnetite (~400 nm); these in turn, show metallic FeNi particles (50−200 nm), with minor amounts of Cu. The two inclusions (AZ1_1 and AZ1_2) were identified by single-crystal X-ray diffraction and electron microprobe analyses as ferropericlase. The two inclusions appear identical in terms of chemistry and texture. Indeed, the polished surface of both inclusions exhibits pervasive, homogeneously distributed nanometer-sized exsolutions of magnetite (with negligible amounts of Al and Mg), which represents ~6% of the total area (*SI Appendix*, Fig. S1); see Materials and Methods below. These exsolutions were initially identified as magnesioferrite (25) but after TEM-EDS analyses were performed, they were revealed to be pure magnetite (Fig. 2 and *SI Appendix*, Fig. S2). The average size of the magnetite exsolutions is ~400 nm and they often coalesce in chains of 2-3 µm length (Fig. 2). Preliminary analyses provided a composition of $(Mg_{0.61}Fe_{0.39})O$ for inclusion AZ1_1 and $(Mg_{0.59}Fe_{0.41})O$ for AZ1_2. Due to the identical microstructure and chemistry of the two inclusions, (25) focused on inclusion AZ1_1 only, for which these authors determined the minimum entrapment pressure by elasto-plastic geobarometry. Chemical analyses were carried out on the inclusion (40 spots, see Materials and Methods). The average chemical composition of ferropericlase was confirmed to be very close to that determined by FEG-SEM, i.e. $(Mg_{0.580}Fe_{0.412})O$, with minor amounts of Mn (0.003 p.f.u.), Ni (0.003 p.f.u.) and Cr (0.001 p.f.u.) (*SI Appendix*, Table S1). Si, Al, Na, Ti, Cu were below the detection limit. We can approximate the composition of the AZ1_1 inclusion as $(Mg_{0.60}Fe_{0.40})O$.

Both FEG-SEM and HAADF-TEM investigations using Z-contrast imaging parameters revealed that, besides the spinel-structured grains, small particles have a brighter contrast than magnetite, implying enrichment in heavier elements (Fig. 2). The first two electron-transparent lamellae, cut using the focused ion beam (FIB) technique, were placed on Cu-grids (*SI Appendix*, Fig. S1), providing an explanation of the high Cu content in the first analyzed Ni-bearing particles. To prevent a Cu-signal produced by secondary excitation of the grid, the third lamella (AZ1_1B) was mounted on a Mo grid (Fig. 3) and its analysis confirmed the presence of Cu in the particles. Bright-field images combined with TEM-EDS element distribution of AZ1_1B are presented in Fig. 3. A bright-field image of a portion of the ferropericlase inclusion containing different types of exsolutions is shown in Fig. 3a, whereas Figs. 3b, c, d, h details the element distribution for Fe, Mg, Cu, Cr, Al, O and Ni, respectively. On the right side of the same figure, three EDS spectra of ferropericlase (green), magnetite (red) and the third phase, which is a FeNi(Cu) alloy (blue), are shown. The HAADF-TEM

image of magnetite trapped in ferropericlase is morphologically similar (Fig. 2) to the "pearl necklaces" of magnesioferrite described in Refs. (21, 23). Furthermore, the bright blebs, whose dimensions are about 5 nm × 80 nm, are composed of Fe and Ni with minor Cu, while O is absent (Fig. 3). The absence of oxygen implies a metallic nature of the FeNi particles. These contain variable minor amounts of Cu, and traces of Al and Cr, as indicated in the TEM compositional maps (Fig. 3). The average composition of the metallic particles – neglecting Al and Cr due to their very low concentrations and basing on the EDS spectra measured on the lamella mounted on molybdenum – is $Fe_{0.71}Ni_{0.24}Cu_{0.05}$.

Figure 4 shows the electron diffraction patterns and high-resolution TEM images obtained on all three phases presented in Fig. 2. The figure provides an overview of the orientation relationships between the ferropericlase matrix, magnetite grains and FeNi(Cu) particles. The bright field image shows the distribution of magnetite in ferropericlase (Fig. 4a). Magnetite exsolutions often align along trails or chains. Fig. 4b shows a high-resolution TEM image of ferropericlase and magnetite, their diffraction pattern is displayed in Fig. 4c. The pattern shows clear topotaxy with $<111>_{magnetite}$ coincident with $<111>_{ferropericlase}$. Fig. 4d shows a region where the three phases are coexisting together. Finally, Figures 4e, g, h show the Fourier transformations of the indicated regions, while Fig. 4f shows a selected area diffraction pattern of the whole region, confirming that the identified phases are ferropericlase, magnetite and FeNi(Cu) alloy. The best indexing match of the FeNi(Cu) alloy TEM diffraction pattern provides a cubic symmetry with unit-cell parameter a = 3.617 Å, which corresponds to a volume V = 47.32 Å^3. The additional diffraction peaks, that belong neither to ferropericlase nor to magnetite, and are not the direct diffraction peak of FeNi(Cu), arise due to double diffraction in the small sized FeNi(Cu) and magnetite particles. Double diffraction is typical in epitactic multi-phase systems. The streaks in the $(1\bar{1}1)$ reciprocal direction at the 002 FeNi(Cu) reflection indicate that the particle is facetted, thus it is little extended perpendicular to the $(1\bar{1}1)$ plane. Generally, our diffraction and imaging work indicates that the particles shapes are defined by well-developed {111} planes with minor development of the {100} planes. Although we cannot exclude twinning in the FeNi(Cu) particle reported in Fig. 4 – twinning was indeed observed in some FeNi(Cu) particles as well as in magnetite (*SI Appendix*, Figs. S3 and S4) – we prefer the simplest possible solution (i.e., "double diffraction") to explain our observations.

Discussion

Recent experimental studies have led to the discovery of new crystalline phases with Fe_xO_y stoichiometry, stable over a wide range in P-T-fo_2 space, whose stability during decompression as well as their potential existence within the Earth are not yet proven. Theoretical considerations and experimental evidence indicates FeNi metal saturation below 250 (±30) km (9, 37–40) as a result of the decreasing fo_2 with depth and pressure effects leading to the disproportionation reaction at the expense of Fe^{2+} to form Fe^{3+}-bearing minerals + Fe(Ni) alloy (41). Experimental studies show that the ferropericlase equilibrated with Fe metal has a Fe/(Fe+Mg) (Fe#) of ~0.20 and NiO contents of ~0.5 wt% (42). In contrast, the ferropericlase inclusion studied here has a Fe# of 0.41 and contains 0.4 wt% NiO. This composition is in good agreement with the worldwide composition of ferropericlase inclusions such as those from Guaniamo (Venezuela), but differs from the predicted primordial composition (42). This variation might indicate that ferropericlase is not

equilibrated at mantle conditions; rather it crystallized upon decomposition from a different precursor, prior to or simultaneously with entrapment in the diamond host (19). We suspect, therefore, that the presence of magnetite trapped in ferropericlase can have a direct link with the local mineralogy and redox state of the deep mantle. We suggest that a series of exsolution reactions is required to explain the presence of magnetite and FeNi alloy from ferropericlase.

Further, assuming a pure Fe_3O_4 composition for magnetite (as only negligible Mg and Al were detected by TEM-EDS, see Fig. 2 and *SI Appendix*, Fig. S2), a normalized composition for the FeNi(Cu) alloy of $Fe_{0.71}Ni_{0.24}Cu_{0.05}$ (the composition of the alloy particles measured by TEM using a Mo grid) and a magnetite: metal ratio of ~6:1 (as measured from both FEG-SEM and TEM images), we can reconstruct the bulk chemistry of the precursor. The result is a phase with stoichiometry of either $(Fe^{3+}_{2.15}Fe^{2+}_{1.59}Ni^{2+}_{0.17}Cu^{+}_{0.04})_{\Sigma=3.95}O_5$ (using a basis of 5 oxygen atoms), or $(Fe^{3+}_{2.57}Fe^{2+}_{1.91}Ni^{2+}_{0.21}Cu^{+}_{0.04})_{\Sigma=4.73}O_6$ (using a basis of 6 oxygen atoms). From this analysis and based on charge, it is evident that the Fe_4O_5 phase is favored relative to Fe_5O_6 as the ideal stoichiometry. However, given the uncertainties, both Fe_4O_5 and Fe_5O_6 are potential candidates to explain the exsolution from ferropericlase that ultimately decomposed to an assemblage of magnetite + FeNi(Cu) metal. A similar equally valid calculation could be performed also for the recently discovered Fe_7O_9 phase, which is very close to Fe_4O_5 in stoichiometry, but given the very limited information concerning its stability field (32) we do not consider it in the further discussion.

Recent experimental studies of the stability fields of these phases as a function of pressure, temperature and fO_2 can be used to evaluate the most plausible oxides (35, 36). These studies point out that both Fe_4O_5 and Fe_5O_6 are stable phases over a wide range of conditions, from upper to lower mantle. At the minimum *P-T* conditions of crystallization of the ferropericlase investigated here (i.e., 15.7 (±2.5) GPa at 1830 (±45) K, (25)), both experimental studies support the stability of Fe_4O_5 relative to Fe_5O_6, irrespectively of the initial Fe content (36) and the Fe/Mg (35) of the bulk rock. The possibility that Fe_4O_5 is an oxide originally exsolved from ferropericlase is further supported by fO_2 calculations. The stability of Fe_4O_5 would require an fO_2 at least above the EMWD (enstatite + magnetite = wadsleyite + diamond) buffer by ~2 log units, which is above the fO_2 at which diamond and carbonate coexist along with clinoenstatite and wadsleyite (11, 35). Such oxidized conditions are not surprising as they have been invoked to explain the variability of Fe# in natural ferropericlase (19, 26) and the incorporation of Fe^{3+} in ferropericlase (43) and are more oxidized than those at which elemental Fe would be stable (i.e. below the iron-wüstite buffer). The formation of Fe_4O_5 would thus be a direct consequence of the oxidation of ferropericlase, a natural carrier of ferric iron.

We thus propose that ferropericlase first formed and was trapped as a single phase during the growth of the diamond (i.e., as a syngenetic inclusion) by redox reactions with the surrounding C-O(-H) fluid (6, 19, 23). In the presence of carbonated fluids, the fO_2 must have been such that ferropericlase oxidized to incorporate relatively high Fe^{3+} contents (~2–10% is a reasonable range from literature data (11, 24, 43, 44)). The exsolution of an Fe^{3+}-rich iron oxide then occurred due to a decrease in the solubility of Fe^{3+} in ferropericlase as the conditions changed. At room pressure and 1273 K the $Fe^{3+}/\sum Fe$ ratio of $(Mg_{0.8}Fe_{0.2})O$ reaches a maximum of approximately 44% at an fO_2 where it coexists with magnesioferrite (45). This maximum level of

Fe^{3+} (solubility), however, decreases with MgO content, pressure and temperature. For a ferropericlase with a nominal composition of $(Mg_{0.60}Fe_{0.40})O$, room pressure data imply a maximum $Fe^{3+}/\sum Fe_{tot}$ ratio closer to 25% (46). The formation at pressures above 8 GPa of iron oxides with stoichiometries that lie between wüstite and magnetite should result in lower $Fe^{3+}/\sum Fe_{tot}$ ratios in wüstite and ferropericlase because the stability fields of the high-pressure oxides extend to lower oxygen fugacities compared to magnetite (35). High-pressure experiments also seem to indicate generally lower ferropericlase $Fe^{3+}/\sum Fe$ ratios at transition zone conditions. Ref. (45) for example determined a $Fe^{3+}/\sum Fe_{tot}$ ratio of 0.074 for $(Mg_{0.8}Fe_{0.2})O$ ferropericlase at 18 GPa and 1273 K at an oxygen fugacity buffered by Re and ReO_2, which should render an oxygen fugacity close to the solubility level (35). Calculations indicate that at the entrapment pressure of the inclusion studied (which likely also partitioned Ni and Cu), Fe_4O_5 should be the phase that would exsolve once the ferropericlase Fe^{3+} solubility limit was exceeded (35). The latter phase presumably also partitioned significant Ni and Cu as it formed. Below 8 GPa magnetite is experimentally demonstrated to be the stable phase (35, 36). In addition, magnetite lamellar intergrowths in Fe_4O_5 in samples recovered to ambient pressures have been reported (36). We interpret the final exsolution of the FeNi(Cu) metal alloy as having occurred subsequently as the diamond cooled to temperatures < 873 K where the Fe_4O_5 (possibly but not necessarily coexisting with magnetite) became unstable (47). The decompression and cooling of the diamond must have occurred rapidly because of the apparent insufficient time for the high-pressure iron oxide to re-equilibrate with the surrounding ferropericlase after. Current estimates of the ascent rate of CO_2-rich magmas, which are candidates to carry diamond samples from the mantle to the surface, are in the range of 300–1850 $m \cdot year^{-1}$ becoming eventually faster as these melts start channeling (48).

In this study, nanometric textural observations along with quantitative chemical and structural analyses lead to the identification of inclusions that appear to have grown through a multi-stage process, starting with the entrapment of a single Fe^{3+} bearing ferropericlase inclusion. After entrapment the exsolution of a high-pressure mixed valence iron oxide, most likely Fe_4O_5, occurred as a result of changing conditions leading to a decrease in the Fe^{3+} solubility in ferropericlase. Fe_4O_5 would, therefore, be formed through the reaction,

$$2FeO + Fe_2O_3 = Fe_4O_5 \quad (1)$$

ferropericlase H-P oxide

An increase in fo_2 is unlikely to have caused this exsolution once the inclusion was trapped within the diamond. Potential causes are, therefore, either an increase in pressure or a decrease in temperature (28, 45-47). Upon decompression below 8 GPa Fe_4O_5, decomposes to wüstite and magnetite (35) as follows:

$$Fe_4O_5 = FeO + Fe_3O_4 \quad (2)$$

H-P oxide wüstite magnetite

On further cooling towards room temperature, after emplacement in the crust, wüstite becomes unstable and metallic Fe(Ni) forms through the reaction (47).

$$4FeO = Fe_3O_4 + Fe \quad (3)$$

293 wüstite magnetite metal alloy with nickel and other siderophile elements also partitioning into the metallic
294 phase.
295
296 Earlier studies (16, 19, 21–24) have identified the phase that exsolved from ferropericlase inclusions as
297 magnesioferrite. However, there is no clear mechanism through which metal should form from
298 magnesioferrite without reducing the fo_2, which seems unlikely once the inclusion is trapped. Because these
299 are physically isolated from the rocks surrounding the diamond crystals, we propose that the metal forms as
300 decomposition product of Fe_4O_5 during decompression.
301
302 In conclusion, we investigated a Fe^{3+}-bearing ferropericlase inclusion trapped in a super-deep diamond that
303 shows FeNi(Cu) metallic particles in close spatial relation with nearly pure magnetite grains. These
304 observations can be explained by: 1) formation of Fe_4O_5 by exsolution upon cooling; 2) decomposition of
305 Fe_4O_5 into wüstite and magnetite; 3) further exsolution of a FeNi(Cu) metal alloy. The previously unknown
306 petrological process documented here may also be applicable to the interpretation of certain xenolith suites,
307 such as pyroxene-ilmenite intergrowths sampled from kimberlites, as these form by decompression
308 exsolution from lower mantle Ca-Ti-Si perovskite (50). This study calls for detailed further investigations of
309 ferropericlase inclusions in other such diamond samples where either the presence of magnetite and/or
310 magnesioferrite has been reported as potential residual of Fe_xO_y phases. Finding additional examples with
311 the features observed in our sample will not only further clarify the origin of the Fe_xO_y phases, but also shed
312 light on previously unobserved petrological deep-Earth processes.
313
314 **Materials and Methods**
315
316 **Sample.** The diamond investigated in this study (Fig. 1) is a flattened colorless dodecahedron recovered
317 from alluvial deposits of the São Luiz River, in the Juina area of Mato Grosso State, Brazil (see also (16,
318 17)). The sample contains two main black tabular inclusions, identified as ferropericlase [$(Mg_{0.60}Fe_{0.40})O$] by
319 single-crystal X-ray diffraction. The smaller inclusion's (AZ1_1) longest dimension is ~160 µm; the larger
320 one's (AZ1_2) is ~340 µm. The diamond host and the two inclusions were investigated previously in (25).

321 **Scanning Electron Microscopy.** The two ferropericlase inclusions were first extracted by mechanical
322 crushing of the host, then polished in a three-steps process and finally carbon coated. FEG-SEM
323 measurements were carried out at the Department of Physics and Astronomy (University of Padova), using a
324 Zeiss SIGMA HD FEG-SEM microscope operating at 20 kV, with a spot size of ~1 nm. Imaging was
325 performed using an InLens secondary electron detector. Compositional analysis was performed using an
326 energy dispersive X-ray spectrometer (EDS by Oxford Instruments). The spatial resolution in microanalysis
327 was of ~1 µm.

328 **Electron probe microanalysis.** Chemical analyses were carried out using a CAMECA SX50 electron
329 microprobe at the Electron Microprobe Laboratory of the CNR Institute of Geosciences and Earth Resources
330 (IGG), hosted by the Department of Geosciences of University of Padova. The analyses were conducted
331 using wavelength-dispersive spectroscopy (WDS) and an accelerating voltage of 20 kV, probe beam current
332 of 20 nA, and a 2 µm beam diameter. Standards (analyzer crystal, element, emission line) used were MgO

(TAP, Mg*K*α); diopside (TAP, Si*K*α); Al_2O_3 (TAP, Al*K*α); $MnTiO_3$ (LIF, Mn*K*α); Cr_2O_3 (LIF, Cr*K*α); Fe_2O_3 (LIF, Fe*K*α); NiO (LIF, Ni*K*α); Cu (LIF; Cu*K*α). We have collected 40 chemical analyses over the AZ_1 inclusion. Analytical data are reported in *SI Appendix*, Table S1.

Transmission Electron Microscopy. Samples for transmission electron microscopy (TEM) where prepared using the FEI Scios dual beam device at Bayerisches Geoinstitut (BGI, University of Bayreuth). The lamellae were cut specifically from locations previously identified in the FEG-SEM. Note that samples AZ1_1A and AZ1_2 were attached to an Omniprobe® Cu-grid, while sample AZ1_1B (on which we collected the data shown in Fig. 3) was mounted on a Mo grid in order to discriminate the real presence of Cu (see the main text).

The FEI Titan™ G2 80–200 microscope at BGI was used for nm-scale characterization. We combined conventional TEM, high resolution (HR)-TEM as well as scanning (S)-TEM modes. The acceleration voltage was set to 200 kV; Energy Dispersive X-ray (EDS) analyses were performed in STEM mode. The probe size after careful optimization is 160 pm, and the final image resolution is a convolution of pixel and probe size. For imaging we acquired BF, ADF and HAADF signals. The HAADF was optimized to yield Z-contrast. EDS spectra were acquired using a windowless SuperX-EDS detector with 4 Si-drift detectors (SDDs) inclined towards the sample in a superimposed circle, resulting in 0.7 srad solid angle. The pixels have sizes of 2 nm.

Acknowledgments

This investigation was financially supported by the project INDIMEDEA, funded by a European Research Council Starting Grant (ERC-StG) 2012 to F.N. (grant 307322). C.A. acknowledges financial support through a Canada Excellence Research Chair (CERC) grant to D.G.P. and the Diamond Exploration and Research Training School (DERTS). K.M. acknowledges financial support through grant MA6287/3 and MA6287/6 of the German Science Foundation (DFG). V.S. acknowledges financial support through “Fondi di Ateneo 2016, 2017 and 2018”. L.B. thanks MIUR, project “TEOREM deciphering geological processes using Terrestrial and Extraterrestrial ORE Minerals”, prot. 2017AK8C32. R.J.H. acknowledges support of the A.F. Sloan Foundation through the Deep Carbon Observatory. L. Tauro and N. Michieli are acknowledged for their help in the FEG-SEM sample preparation and analysis, respectively. We are grateful to D. Wiesner and J. Polednia for FIB sample preparation. FEI Scios FIB machine, BGI Bayreuth, is supported through grant INST 91/315-1 FUGG. R. Carampin is thanked for providing technical assistance in the EMPA analyses. S. Castelli is thanked for the picture of the diamond. The DeBeers Group of Companies is thanked for the donation of the diamond to J.W.H.

References

1. T. Stachel, J. W. Harris, The origin of cratonic diamonds — Constraints from mineral inclusions. *Ore Geology Reviews* **34**, 5–32 (2008).

2. M. J. Walter, *et al.*, Deep mantle cycling of oceanic crust: evidence from diamonds and their mineral inclusions. *Science* **334**, 54–57 (2011).

3. D. G. Pearson, *et al.*, Hydrous mantle transition zone indicated by ringwoodite included within diamond. *Nature* **507**, 221–224 (2014).

4. E. M. Smith, *et al.*, Large gem diamonds from metallic liquid in Earth's deep mantle. *Science* **354**, 1403–1405 (2016).

5. F. Nestola, *et al.*, $CaSiO_3$ perovskite in diamond indicates the recycling of oceanic crust into the lower mantle. *Nature* **555**, 237–241 (2018).

6. A. R. Thomson, M. J. Walter, S. C. Kohn, R. A. Brooker, Slab melting as a barrier to deep carbon subduction. *Nature* **529**, 76–79 (2016).

7. E. M. Smith, *et al.*, Blue boron-bearing diamonds from Earth's lower mantle. *Nature* **560**, 84–87 (2018).

8. O. Tschauner, *et al.*, Ice-VII inclusions in diamonds: Evidence for aqueous fluid in Earth's deep mantle. *Science* **359**, 1136–1139 (2018).

9. D. J. Frost, *et al.*, Experimental evidence for the existence of iron-rich metal in the Earth's lower mantle. *Nature* **428**, 409–412 (2004).

10. M. J. Walter, *et al.*, Primary carbonatite melt from deeply subducted oceanic crust. *Nature* **454**, 622–625 (2008).

11. V. Stagno, *et al.*, The stability of magnesite in the transition zone and the lower mantle as function of oxygen fugacity. *Geophysical Research Letters* **38** (2011).

12. F. Kaminsky, Mineralogy of the lower mantle: A review of "super-deep" mineral inclusions in diamond. *Earth-Science Reviews* **110**, 127–147 (2012).

13. V. Stagno, Carbon, carbides, carbonates and carbonatitic melts in the Earth's interior. *J. Geol. Soc. London* **176**, 375–387 (2019).

14. V. Stagno, *et al.*, Carbon-bearing phases throughout Earth's interior. *Deep Carbon*, 66–88 (2019).

15. L. Stixrude, C. Lithgow-Bertelloni, Geophysics of chemical heterogeneity in the mantle. *Annual Review of Earth and Planetary Sciences* **40**, 569–595 (2012).

16. B. Harte, J. W. Harris, M. T., Hutchison, G. R. Watt, M. C. Wilding, Lower mantle mineral associations in diamonds from Sao Luiz, Brazil. Mantle petrology: Field observations and high-pressure experimentation: A tribute to Francis R. (Joe) Boyd, **6**, 125-153 (1999).

17. P. C. Hayman, M. G. Kopylova, F. V. Kaminsky, Lower mantle diamonds from Rio Soriso (Juina area, Mato Grosso, Brazil). *Contributions to Mineralogy and Petrology* **149**, 430–445 (2005).

18. L.-G. Liu, An alternative interpretation of lower mantle mineral associations in diamonds. *Contributions to Mineralogy and Petrology* **144**, 16–21 (2002).

19. P. Nimis, Trapped minerals under stress. *Geology* **46**, 287–288 (2018).

20. F. Zhu, *et al.*, Kinetic control on the depth distribution of superdeep diamonds. *Geophysical Research Letters* **46**, 1984–1992 (2019).

21. R. Wirth, L. Dobrzhinetskaya, B. Harte, A. Schreiber, H. W. Green, High-Fe (Mg, Fe)O inclusion in diamond apparently from the lowermost mantle. *Earth and Planetary Science Letters* **404**, 365–375 (2014).

22. F. V. Kaminsky, *et al.*, Oxidation potential in the Earth's lower mantle as recorded by ferropericlase inclusions in diamond. *Earth and Planetary Science Letters* **417**, 49–56 (2015).

23. M. Palot, *et al.*, Evidence for H_2O-bearing fluids in the lower mantle from diamond inclusion. *Lithos* **265**, 237–243 (2016).

24. F. Nestola, *et al.*, Synchrotron Mössbauer Source technique for in situ measurement of iron-bearing inclusions in natural diamonds. *Lithos* **265**, 328–333 (2016).

25. C. Anzolini, *et al.*, Depth of diamond formation obtained from single periclase inclusions. *Geology* **47**, 219–222 (2019).

26. F. V. Kaminsky, R. Wirth, A. Schreiber, A microinclusion of lower-mantle rock and other mineral and nitrogen lower-mantle inclusions in a diamond. *The Canadian Mineralogist* **53**, 83–104 (2015).

27. D. Nishio-Hamane, Fe^{3+} and Al solubilities in $MgSiO_3$ perovskite: implication of the $Fe^{3+}AlO_3$ substitution in $MgSiO_3$ perovskite at the lower mantle condition. *Geophysical Research Letters* **32** (2005).

28. M. Longo, C. A. McCammon, S. D. Jacobsen, Microanalysis of the iron oxidation state in (Mg,Fe)O and application to the study of microscale processes. *Contributions to Mineralogy and Petrology* **162**, 1249–1257 (2011).

29. B. Lavina, *et al.*, Discovery of the recoverable high-pressure iron oxide Fe_4O_5. *Proc. Natl. Acad. Sci. U. S. A.* **108**, 17281–17285 (2011).

30. A. B. Woodland, D. J. Frost, D. M. Trots, K. Klimm, M. Mezouar, In situ observation of the breakdown of magnetite (Fe_3O_4) to Fe_4O_5 and hematite at high pressures and temperatures. *American Mineralogist* **97**, 1808–1811 (2012).

31. B. Lavina, Y. Meng, Unraveling the complexity of iron oxides at high pressure and temperature: Synthesis of Fe_5O_6. *Science Advances* **1**, e1400260 (2015).

32. R. Sinmyo, *et al.*, Discovery of Fe_7O_9: a new iron oxide with a complex monoclinic structure. *Scientific Reports* **6** (2016).

433 33. T. Ishii, L. Uenver-Thiele, A. B. Woodland, E. Alig, T. Boffa Ballaran, Synthesis and crystal structure of
434 Mg-bearing Fe_9O_{11}: New insight in the complexity of Fe-Mg oxides at conditions of the deep upper
435 mantle. *American Mineralogist* **103**, 1873–1876 (2018).

436 34. A. B. Woodland, *et al.*, Fe_4O_5 and its solid solutions in several simple systems. *Contributions to*
437 *Mineralogy and Petrology* **166**, 1677–1686 (2013).

438 35. R. Myhill, *et al.*, On the P–T– f_{O2} stability of Fe_4O_5, Fe_5O_6 and Fe_4O_5-rich solid solutions. *Contributions*
439 *to Mineralogy and Petrology* **171**, 51 (2016).

440 36. K. Hikosaka, R. Sinmyo, K. Hirose, T. Ishii, Y. Ohishi, The stability of Fe_5O_6 and Fe_4O_5 at high
441 pressure and temperature. *American Mineralogist* **104**, 1356–1359 (2019).

442 37. C. Ballhaus, Is the upper mantle metal-saturated? *Earth and Planetary Science Letters* **132**, 75–86
443 (1995).

444 38. A. Rohrbach, *et al.*, Metal saturation in the upper mantle. *Nature* **449**, 456–458 (2007).

445 39. A. Rohrbach, M. W. Schmidt, Redox freezing and melting in the Earth's deep mantle resulting from
446 carbon–iron redox coupling. *Nature* **472**, 209–212 (2011).

447 40. A. Rohrbach, S. Ghosh, M. W. Schmidt, C. H. Wijbrans, S. Klemme, The stability of Fe–Ni carbides in
448 the Earth's mantle: Evidence for a low Fe–Ni–C melt fraction in the deep mantle. *Earth and Planetary*
449 *Science Letters* **388**, 211–221 (2014).

450 41. D. J. Frost, C. A. McCammon, The Redox State of Earth's Mantle. *Annual Review of Earth and*
451 *Planetary Sciences* **36**, 389–420 (2008).

452 42. A.-L. Auzende, *et al.*, Element partitioning between magnesium silicate perovskite and ferropericlase:
453 New insights into bulk lower-mantle geochemistry. *Earth and Planetary Science Letters* **269**, 164–174
454 (2008).

455 43. K. Otsuka, M. Longo, C. A. McCammon, S.-I. Karato, Ferric iron content of ferropericlase as a function
456 of composition, oxygen fugacity, temperature and pressure: Implications for redox conditions during
457 diamond formation in the lower mantle. *Earth and Planetary Science Letters* **365**, 7–16 (2013).

458 44. C. A. McCammon, T. Stachel, J. W. Harris, Iron oxidation state in lower mantle mineral assemblages.
459 *Earth and Planetary Science Letters* **222**, 423–434 (2004).

460 45. C. McCammon, J. Peyronneau, J.-P. Poirier, Low ferric iron content of (Mg,Fe)O at high pressures and
461 temperatures. *Geophysical Research Letters* **25**, 1589–1592 (1998).

462 46. D. H. Speidel, Phase Equilibria in the System MgO-FeO-Fe_2O_3: The 1300 °C isothermal iection and
463 extrapolations to other temperatures. *Journal of the American Ceramic Society* **50**, 243–248 (1967).

464 47. B. Sundman, An assessment of the Fe-O system. *Journal of Phase Equilibria* **12**, 127–140 (1991).

48. V. Stagno, V. Stopponi, Y. Kono, C. E. Manning, T. Irifune, Experimental determination of the viscosity of Na2CO3 melt between 1.7 and 4.6 GPa at 1200–1700 °C: Implications for the rheology of carbonatite magmas in the Earth's upper mantle. *Chemical Geology* **501**, 19–25 (2018).

49. C. A. McCammon, I. L. Chinn, J. J. Gurney, M. E. McCallum, Ferric iron content of mineral inclusions in diamonds from George Creek, Colorado determined using Mössbauer spectroscopy. *Contributions to Mineralogy and Petrology* **133**, 30–37 (1998).

50. K. D. Collerson, H. Terasaki, E. Ohtani, A. Suzuki, T. Kondo, A lower mantle origin for megacryst suite pyroxene–ilmenite xenoliths in kimberlites: high-pressure experimental constraints and geodynamic significance. *EOS Transactions of the American Geophysical Union* **85**, Fall Meeting Supplement, Abstract U41A-0705 (2004).

Figures and Tables

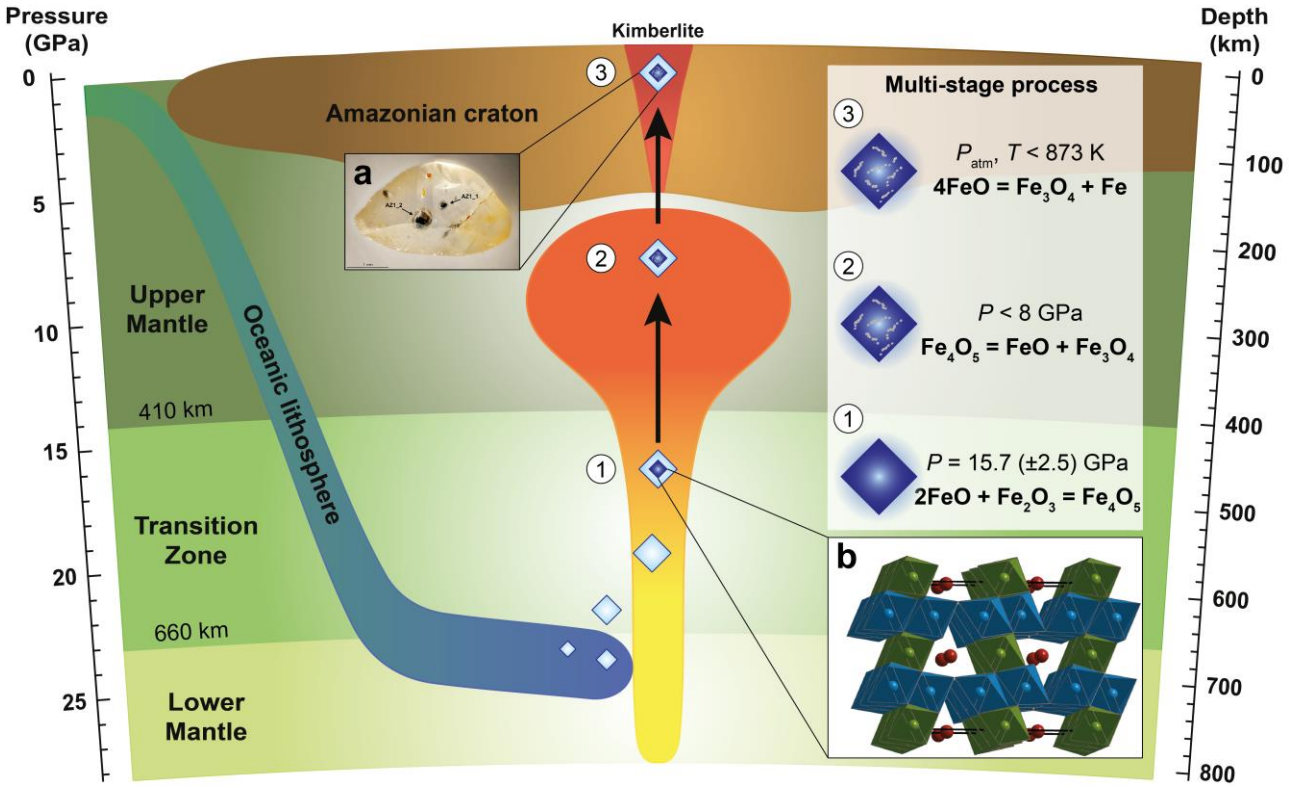

Figure 1. Schematic of FeNi(Cu) inclusions formation through a multi-stage process during diamond exhumation: 1) at 15.7 (±2.5) GPa Fe_4O_5 exsolves from FeO as the Fe^{3+} solubility is exceeded due to decompression; 2) below 8 GPa Fe_4O_5 decomposes to almost pure wüstite and magnetite; 3) at room *P* and *T* < 873 K wüstite becomes unstable and FeNi(Cu) metal alloy forms. a) Photograph of the inclusion-bearing diamond studied in this work (the longest dimension is 4 mm, Ref. (25)). b) Crystal structure of Fe_4O_5 viewed along the *a* axis (from Ref. (29)), where green and blue octahedra represent sites Fe1 and Fe2, respectively, whereas red spheres represent site Fe3.

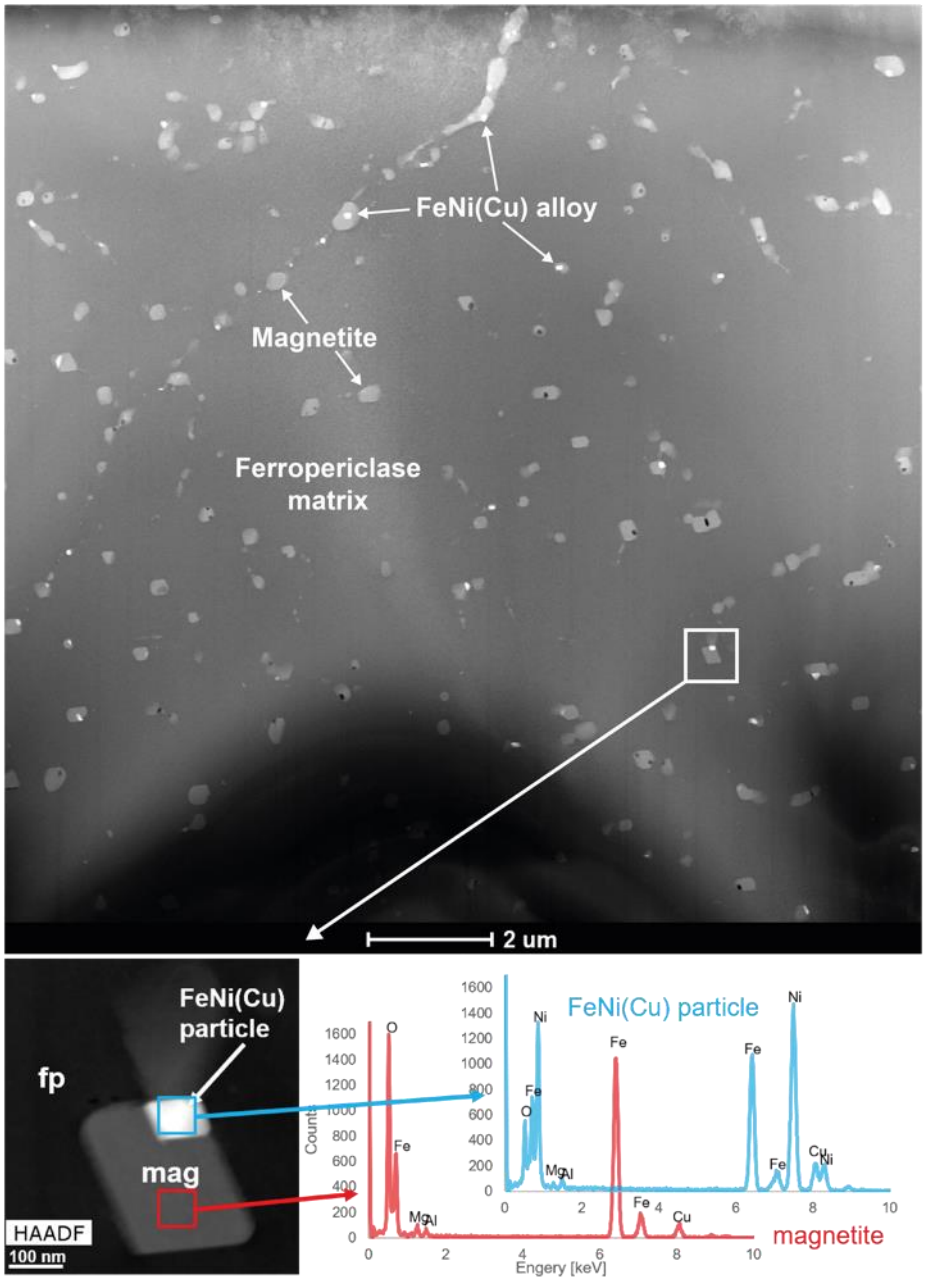

Figure 2. HAADF STEM image of sample AZ1_2 mounted on a copper TEM grid, showing Z-contrast: brighter regions have a higher average atomic number, while darker regions have a lower average atomic number. The dark matrix is ferropericlase, whereas grey grains represent magnetite. Bright spots are FeNi(Cu) particles. The original spectra are deconvolved and background corrected, the display is not quantitative.

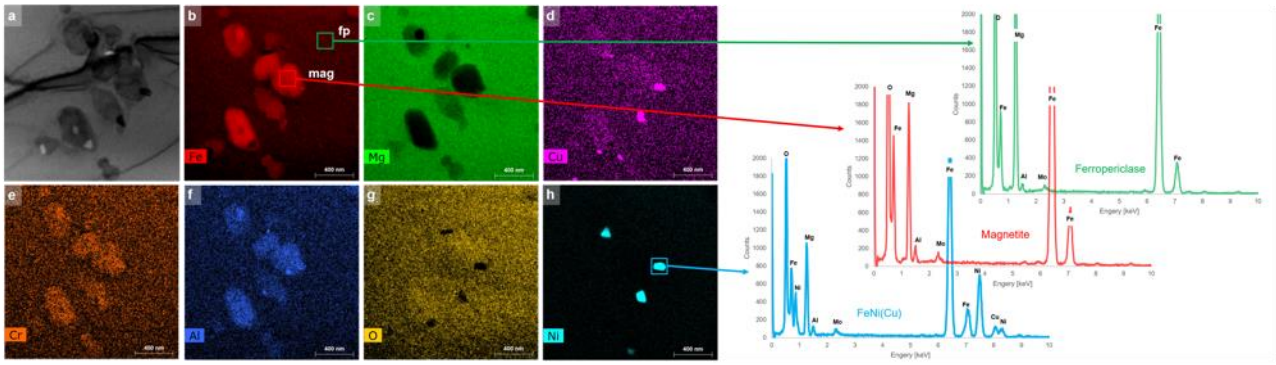

Figure 3. Element distribution maps in the ferropericlase (fp), magnetite (mag) and FeNi(Cu) particles on sample AZ1_1B mounted on a molybdenum TEM grid. a) Bright field micrograph. b)-h) Element distributions of the elements indicated in the lower left corner, the original spectra are deconvolved and background corrected; the display is not quantitative. Note the spatially positively correlated distribution of Fe-Al-Cr inversely correlated to Mg. While the distribution of Cu and Ni is in places positively correlated or not at all correlated.

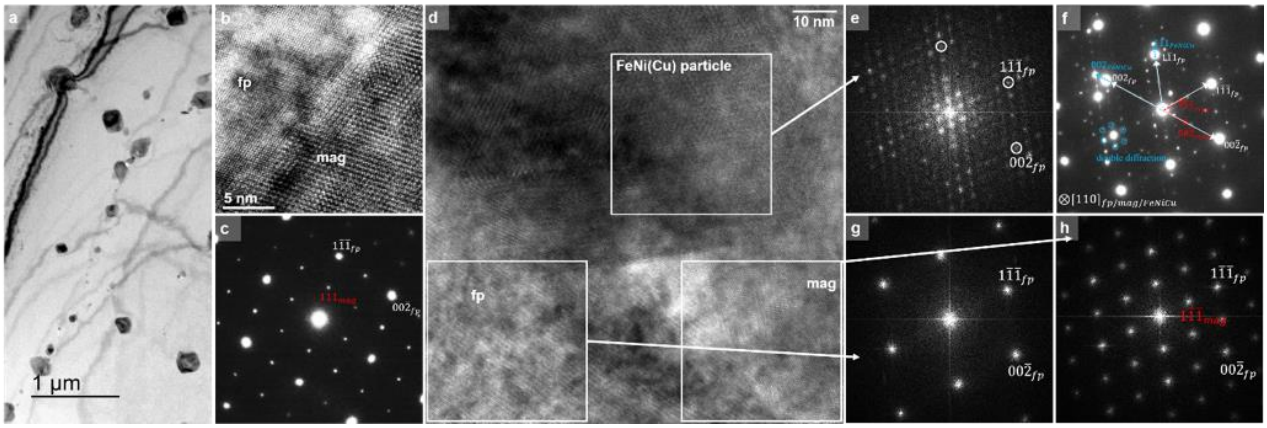

Figure 4. Overview on the orientation relationships between fp, mag and the FeNi(Cu) particles. a) Bright field of the general distribution of magnetite in ferropericlase. The magnetite exsolutions often aligned along trails or chains. b) HRTEM. Ferropericlase in the upper left corner and magnetite in the lower right corner. c) Selected area diffraction pattern of fp and mag. The well-known topotaxy is revealed (the general direction {111} mag parallel {111} fp). d) HRTEM of a relatively thick region containing fp, mag and a FeNi(Cu) particle. e)-g)-h) are Fourier transformations of the indicated regions, while f) is a selected area diffraction pattern of the whole region. The primary diffraction peaks are identified as fp (white arrows), mag (red arrows) and FeNi(Cu) (blue arrows). The additional peaks that do neither belong to fp, mag, or FeNi(Cu) arise from double diffraction. The primary electron beam is re-diffracted by the small sized FeNi(Cu) and magnetite particle, they are exemplarily indicated in blue. They repeat around many primary diffraction peaks. Note the streaks in the $(1\bar{1}1)$ reciprocal direction associated to the 002 FeNi(Cu) reflection.